Dalton Transactions

Accepted Manuscript

ROYAL SOCIETY OF CHEMISTRY

www.rsc.org/dalton

Journal Name

ARTICLE

Ag_3PO_4 nanoparticles loaded on 3D flower-like spherical MoS_2: Highly efficient hierarchical heterojunction photocatalyst

Received 00th January 20xx,
Accepted 00th January 20xx

DOI: 10.1039/x0xx00000x

www.rsc.org/

Li Wang[a], Yuanyuan Chai[a], Jia Ren[a], Jing Ding[a], Qianqian Liu [a], Wei-Lin Dai[a]*

Novel 3D hierarchical Ag_3PO_4/MoS_2 composites were successfully prepared through a facile and reproducible hydrothermal-in situ precipitation method. The 3D flower-like spherical MoS_2 nanoarchitectures acted as an excellent supporting matrix for the in situ growth of Ag_3PO_4 nanoparticles. The photocatalytic performance of the composites and the effect of the amount of MoS_2 were investigated. The obtained hierarchical Ag_3PO_4/MoS_2 composites exhibited significantly enhanced performance for photocatalytic oxidation of Rhodamine B (RhB) compared with pure Ag_3PO_4 under visible light irradiation. Ag_3PO_4/MoS_2 composite with 15wt% of MoS_2 showed the optimal photoactivity for the degradation of RhB, which was approximately 4.8 times as high as that of pure Ag_3PO_4. What's more, the optimal Ag_3PO_4/MoS_2 composite also showed better photodegradation efficiency for methyl orange (MO) and p-chlorophenol (4-CP) than pure Ag_3PO_4. More attractively, the stability of Ag_3PO_4 was improved after the in situ deposition of Ag_3PO_4 particles on the surface of MoS_2 nanoflakes due to the conductivity of MoS_2 itself as electron acceptors. The enhanced performance of the hierarchical Ag_3PO_4/MoS_2 composites under visible light was caused by a synergistic effect including the improved separation of photogenerated charge carriers, boosted light harvesting, relatively high surface area and matching energy band structure between the two components. Interestingly, the heterostructured Ag_3PO_4/MoS_2 composite reduced the use of the noble metal silver, thereby effectively reducing the cost of the Ag_3PO_4 based photocatalyst. Ultimately, a MoS_2 involved photocatalytic mechanism for the hierarchical Ag_3PO_4/MoS_2 composites was also proposed.

1. Introduction

Given the increasingly serious environment and energy problems, semiconductor-based photocatalytic materials, which are applied for decomposition of organic pollutants to retard the deterioration of natural environment and water splitting to produce hydrogen, have caused extensive concerns. [1-2] Compared to the conventional strategies for environmental remediation, photocatalysis is a better choice to settle the energy and pollution issues owing to the efficient and eco-friendly features. During the past decades, TiO_2 semiconductor has been widely used as a classic photocatalyst in several fields. [3] Nevertheless, TiO_2 with a relatively broad band gap (~3.20 eV) can only be excited by ultraviolet light merely accounting for less than 5% of the solar spectrum, and the separation efficiency of photogenerated electron-hole pairs is comparatively low. [4-5] These factors restrict its practical applications. Consequently, it's imperative to design and prepare novel highly efficient and stable visible-light-driven photocatalysts.

Recently, a series of novel visible-light-responsive photocatalysts with narrow band-gap have been reported, such as modified TiO_2 [6-7], CdS [8], WO_3 [9], Bi_2XO_6 (X=W, Mo) [10-11], Cu_2O [12], $BiVO_4$ [13], BiOX (X=Br, I) [14-15] and g-C_3N_4 [16-18], etc. Among them, Ag-containing compounds, such as Ag_2O [19], Ag_2S [20], Ag_2CO_3 [21], AgX (X=Br, I) [22-23], Ag_3PO_4 [24], have been proved to be one of the most promising photocatalysts due to their superior utilization rate of visible light and high photocatalytic activity. Especially the Ag_3PO_4 semiconductor, a breakthrough in the photocatalysis field as an highly active photocatalyst for degradation of organic pollutants and water splitting, its quantum efficiency values can reach up to 90% at wavelengths longer than 420 nm. However, Ag_3PO_4 suffers from photocorrsion under prolonged light irradiation due to light-sensitivity and slightly soluble in aqueous solution, and tends to aggregate to form larger particles, which hinder its further application as a recyclable and highly efficient photocatalyst. [25] Hence, it's very essential to develop effective methods to improve the stability and activity of the Ag_3PO_4 photocatalyst. To date, there are mainly two ways to ameliorate the photocatalytic properties. One is designing various Ag_3PO_4 nanostructures, primarily considering its size and morphology effects. [26-27] The other one is coupling Ag_3PO_4 with other semiconductor photocatalysts or conductive materials to form hybrid structures, such as Ag_3PO_4/graphene [28], Ag_3PO_4/Bi_2MoO_6 [29], Ag_3PO_4/WO_3 [30], Ag_3PO_4/CNT [31], Ag_3PO_4/AgBr/Ag [32] Ag_3PO_4/C_3N_4 [33-34], etc. These Ag_3PO_4-based complexes can not only effectively protect the Ag_3PO_4 crystals from dissolution in aqueous solutions, but also enhance their photocatalytic activity and stability through the effective separation of photo-induced charge carriers via the interface of different semiconductors. Thus, as an excellent way to design novel photocatalysts leading to distinctly improvement of photocatalytic performance, modifying Ag_3PO_4 with other matching semiconductors still needs extensive study.

As a kind of graphene-like lamellar structure material, single or multiple-layer 2D transition metal disulfides have received significant attention. Among which, molybdenum disulfide (MoS_2) is the most studied one by virtue of its unique electronic and chemical

properties and a sizable band-gap [35]. Its layered structure consists of hexagonal layers of Mo atoms sandwiched between two layers of S atoms, with a stoichiometry of MoS_2. [36] In most cases, MoS_2 is usually used as a substitute of noble metals for photocatalytic hydrogen evolution, and the deposition of MoS_2 on the surface of the catalysts enhanced the photocatalytic activity. For example, Liu et al. [37] reported that high photoelectrochemical activity for H_2 evolution was obtained by deposition of CdS on the surface of MoS_2 to form p-n heterojunction. Shen et al. [38] prepared a kind of MoS_2 nanosheets/TiO_2 nanowire hybrid nanostructure, which exhibited high activity in visible light photocatalytic hydrogen evolution reaction. Moreover, nanoscale MoS_2 is a reportedly good O_2-activation cocatalyst for oxidation reactions, resulting in more production of superoxide radical anions ($\cdot O_2^-$) during the photo-oxidation process. [1] A number of composite material systems, such as MoS_2/BiOBr [39], MoS_2/SnO_2 [40] and MoS_2/Bi_2MoO_6 [41], have received attention for their high performance in photodegradation of organic pollutants under visible light irradiation.

The 3D structure of MoS_2 has become particularly interesting owing to their enhanced structure complexity and the potential to exploit the functionalities of this material. Because of the relatively narrow band gap (~1.8 eV) of MoS_2 and the matching band potentials between Ag_3PO_4 and MoS_2, it is expected to construct hierarchical Ag_3PO_4/MoS_2 (3D) semiconductor composites with synergistic effect for high photocatalytic capability and stability. Besides, there are few reports based on using 3D graphene-like materials to modify the Ag_3PO_4 semiconductor. Herein, in this work, we demonstrated a facile and reproducible template free in situ precipitation method to prepare the hierarchical Ag_3PO_4/MoS_2 composites, where 3D spherical MoS_2 acted as supporters for the growth of Ag_3PO_4 nanoparticles to raise the visible-light-sensitivity and stability of Ag_3PO_4. The content of 3D spherical MoS_2 in this novel hierarchical composite photocatalyst is optimized. This synthetic method contributed to the formation of junctions among MoS_2 and Ag_3PO_4, and the results displayed that the stability of Ag_3PO_4 was improved under visible light irradiation and a more fascinating photocatalytic activity for decomposition of Rhodamine B (RhB) was observed after hybridization with MoS_2, deriving from the high interfacial charge transfer between these two components. Interestingly, the silver weight percentage of the photocatalysts decreased extensively, thus reducing the cost of Ag_3PO_4 based photocatalysts. The relationship between the specific structure and the enhancement of stability and the admirable photocatalytic activity was investigated. Meanwhile, a possible photocatalytic mechanism for the hierarchical Ag_3PO_4/MoS_2 (3D) composites was also proposed.

2. Experimental

All the reagents purchased from Sinopharm Chemical Reagent Co., Ltd. were of analytical purity and were used as received. The schematic illustration of the synthesis of hierarchical Ag_3PO_4/MoS_2 composites was depicted in Fig. S1†.

2.1 Synthesis of 3D spherical MoS_2 nanoarchitectures

The 3D spherical MoS_2 nanoarchitecture was synthesized in a Teflon-lined autoclave via a hydrothermal route. Briefly, a certain amount of MoO_3 and thioacetamide (TAA) respectively used as Mo and S sources were dissolved in a beaker with 60 mL deionized (DI) water under continuous stirring to form a transparent solution. And then, a given amount of hydroxylammonium chloride ($NH_2OH{\cdot}HCl$) was added into the solution. After being ultrasonicated and magnetically stirred successively, the ivory-white mixture was transferred to a 100 mL Teflon-coated autoclave and held at 180°C for 48 h. The black precipitates formed in the solution were then collected by centrifugation, washed with DI water and ethanol for several times, and finally dried in vacuum oven at 60°C for 12 h for the next stage of the research.

2.2 Fabrication of hierarchical Ag_3PO_4/MoS_2 composites

Ag_3PO_4 nanoparticles coupled with X (X= 10, 15, 20 and 30 wt %) amount of MoS_2 (denoted as Ag_3PO_4/MoS_2-X) were prepared through a facile in situ precipitation method. Typically, an appropriate amount of MoS_2 (30 mg) was dispersed in 20 mL DI water by sonication for 10 min and subsequent agitation for 20 min. To this, 24 mL silver nitrate solution with a concentration of 0.05 M was added and stirred at room temperature for 1 h, followed by dropwise dosing of 8 mL of 0.05 M trisodium phosphate solution. The mixture was stirred for 5 h while precipitates were formed. The obtained solid product was centrifuged, washed with water and ethanol and vacuum-dried at 60°C for 8 h. Other composites containing different weight proportions of 3D spherical MoS_2 could be obtained using the same method. The pure Ag_3PO_4 crystals were also prepared for comparison following the same method without the addition of MoS_2.

2.3 Characterization of the as-prepared photocatalysts

The XRD patterns of the as-prepared samples (2θ ranges from 10° to 90°) were recorded at room temperature with scanning speed of 8° min^{-1} on a Bruker D8 advance spectrometer with Cu *Kα* radiation (λ=0.154 nm), operated at 30 mA and 40 kV. Transmission electron micrographs (TEM) images were obtained on a JEOL 2011 microscope operated at an accelerating voltage of 200 kV. The samples were supported on carbon-coated copper grids for the experiment. The FT-IR spectra were obtained on a Nicolet Avatar-360 FT-IR spectrometer. Nitrogen adsorption-desorption isotherms were measured on a Micromeritics Tristar 3000 system. Samples were degassed at 250°C on a vacumm line for 3 h. Specific surface areas were calculated by utilizing a standard Brunauer-Emmett-Teller (BET) method. Ultraviolet visible (UV-vis) DRS spectra were obtained using a SHIMADZU UV-2450 instrument with a collection speed of 40 nm·min^{-1} using $BaSO_4$ as the reference. X-ray photoelectron spectroscopy (XPS) measurements were performed on a PHI 5000C ESCA System with Mg Kα source at 14.0 kV and 25 mA. All the binding energies were referenced to the contaminant C1s peak at 284.6 eV of the surface adventitious carbon. The photoluminescence (PL) spectra were obtained by using a Hitachi F-4500 Fluorescence spectrophotometer with an excitation wavelength of 360 nm using Xe lamp as excitation source.

2.4 Evaluation of photocatalytic activity

The photocatalytic performance of the as-prepared samples was evaluated through the photodegradation of RhB under visible light. A 300 W Xe arc lamp (CeauLight, CEL-HXF300) equipped with a 420 nm cut-off filter provided visible-light irradiation. In a typical photocatalytic measurement, 0.025 g of the composite was dispersed in 100 mL of an aqueous solution of RhB (10 mg/L) via ultrasonication for 2 min. Before being exposed to light, the suspension was stirred in the dark condition for 30 min to reach an adsorption-desorption equilibrium. During the photocatalytic tests, 3 mL suspensions were sampled at a given time interval, followed by centrifugation at 12000 rpm to remove the photocatalyst. The concentration of RhB in the supernatant was determined by means of a UV-Vis spectrophotometer at a wavelength of 550 nm. The

photodegradation efficiency (E%) was calculated using the following equation:

$$E\ \% = (C_0\text{-}C) / C \times 100\% = (A_0\text{-}A) / A_0 \times 100\%,$$

where C_0 and A_0 are the initial concentration and absorbance of RhB solution at 550 nm while C and A are the concentration and absorbance of RhB solution at 550 nm after visible light irradiation at any time.

Furthermore, the photodegradation of MO (10 mg/L) and 4-CP (10 mg/L) over the optimal hierarchical Ag_3PO_4/MoS_2 composite was performed under the same reaction conditions as those mentioned above. The detection wavelengths for MO and 4-CP were 464 and 225 nm, respectively.

3. Results and discussion

3.1 Catalyst characterization

3.1.1 X-ray diffraction (XRD)

XRD is used to investigate the crystal structure of the samples. Fig. 1 shows the XRD characterizations of Ag_3PO_4, MoS_2 and the obtained Ag_3PO_4/MoS_2-X composites. For pure Ag_3PO_4, the diffraction peaks at 21.7°, 29.7°, 33.3°, 36.5°, 47.8°, 52.6°, 54.9°, 57.2°, 61.8° and 71.8° are respectively ascribed to the (110), (200), (210), (211), (310), (222), (320), (321), (400) and (421) diffraction planes, which are characteristic peaks of the body-centered cubic phase of Ag_3PO_4 (JCPDS: 06-0505) [42]. While for pure 3D spherical MoS_2 nanoarchitectures, the peaks at 13.9°, 33.6°, 39.8° and 59.5° are respectively corresponding to the (002), (100), (103) and (110) diffraction planes of 2H-MoS_2 (JCPDS: 37-1492), which is in well accordance with previous studies [43]. It is unambiguous that the

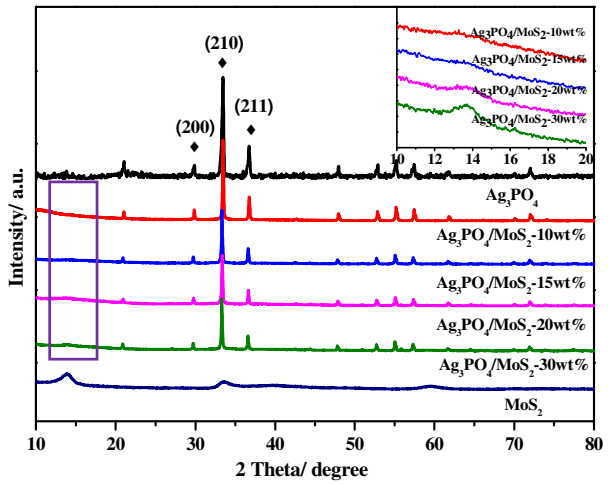

Fig.1 XRD patterns of Ag_3PO_4, MoS_2 and the obtained hierarchical Ag_3PO_4/MoS_2-X composites.

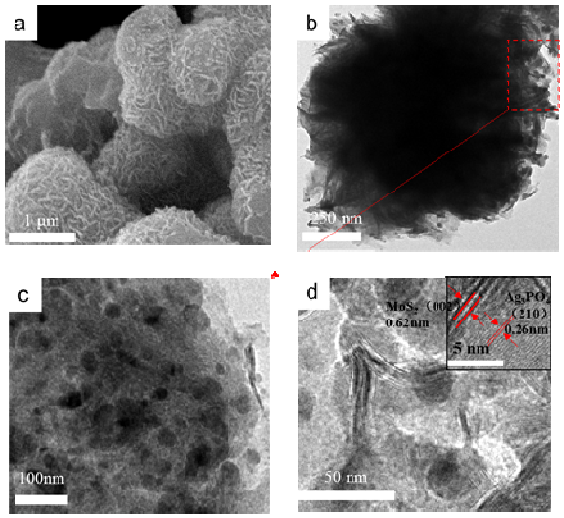

Fig. 2 SEM image (a) of MoS_2, TEM images (b,c) and HRTEM image (d) of 3D hierarchical Ag_3PO_4/MoS_2 composite.

characteristic peaks of Ag_3PO_4 could be found for all as-prepared Ag_3PO_4/MoS_2 samples with different content of MoS_2. Compared to Ag_3PO_4, the intensity of the diffraction peaks of MoS_2 is relatively weak. But from the inset of Fig. 1, it can also distinguish the peaks of MoS_2, suggesting the presence of MoS_2, and it makes sense that the peak intensities increased with the increasing content of MoS_2. Moreover, the addition of MoS_2 did not obviously change the diffraction peak positions of Ag_3PO_4, implying that MoS_2 was not incorporated into the Ag_3PO_4 lattice. Both the XRD patterns of Ag_3PO_4 and MoS_2 can be observed, indicating that Ag_3PO_4 nanoparticles were successfully coated on the surface of 3D MoS_2 support.

3.1.2 Transmission Electron Microscopy (TEM)

The morphology and fine microstructure of the hierarchical Ag_3PO_4/MoS_2 samples is revealed by SEM and TEM. Fig. 2a illustrates the SEM image of the primary 3D spherical MoS_2 nanoarchitectures. From this image, the diameter of 3D MoS_2 flowerlike sphere is about 1 μm to 1.2 μm, and it is easy to observe that the flower-like spherical MoS_2 are actually assembled by several thin flakes. However, after being subjected to the solution of Ag^+ and PO_4^{3-}, the black MoS_2 became yellowish-green in color, indicating the formation of Ag_3PO_4. Fig. 2b displayed a typical TEM image of the as-prepared Ag_3PO_4/MoS_2 hierarchical nanocomposites, where the MoS_2 nanoflakes were fully decorated with uniform Ag_3PO_4 nanoparticles. After deposition of Ag_3PO_4, the spherical morphology of MoS_2 roughly maintained. From Fig. 2c (the magnified section of Fig. 2b), it can be seen that Ag_3PO_4 nanoparticles were evenly distributed across the surface of MoS_2 nanoflakes, and no apparent aggregation of the Ag_3PO_4 nanoparticles was discerned. To further confirm the intimate contact and interfacial junction between Ag_3PO_4 and MoS_2, the sample was characterized by HRTEM, as shown in Fig. 2d. A clear lattice fringe of 0.62 nm ascribed to the (002) plane of MoS_2 could be observed [44], and another set of fringes, with an interplanar distance of about 0.26 nm, corresponded to the (210) lattice plane of Ag_3PO_4 [45]. Thereby, it manifested the formation of a heterojunction structure between Ag_3PO_4 and MoS_2, which was beneficial for the separation of photogenerated charge carriers. According to the energy-dispersive X-ray spectrometry (EDS) in Fig.

S2†, the existence of Ag, P, Mo and S elements in the Ag_3PO_4/MoS_2 composites had been proved. Therefore, the TEM results also confirmed that the hierarchical Ag_3PO_4/MoS_2 composites were successfully developed.

3.1.3 X-ray photoelectron spectroscopy (XPS)

More detailed information regarding the surface chemical composition of the Ag_3PO_4/MoS_2 samples is analyzed by XPS. The binding energies obtained were corrected by referencing the C 1s line to 284.6 eV. Fig. 3a exhibited the full scanned XPS spectra of the hierarchical Ag_3PO_4/MoS_2 composites with 15 wt% of MoS_2, and the survey spectra demonstrated that Mo, S, O, Ag and P elements existed in this materials, which was in consistent with the constituent of this composites. Besides, the atomic ratio of S/Mo was approximately 2, in good agreement with the stoichiometry of MoS_2. The presence of C 1s peak was principally originated from the adventitious carbon on the surface of the as-synthesized composites from gaseous species [46]. As discerned from the XPS spectra of Ag 3d (Fig. 3b), there were two individual peaks at *ca.* 374.0 and 368.1 eV, which could be assigned to $3d_{3/2}$ and $3d_{5/2}$ of typical Ag^+, respectively [47]. In Fig. 3c, a peak at 133.2 eV appeared for P 2p spectra, corresponding to P^{5+} coming from Ag_3PO_4 [44]. For the Mo 3d XPS spectra shown in Fig. 3d, two kind of binding energies locating at 232.3 and 229.1 eV could be respectively attributed to Mo $3d_{3/2}$ and $3d_{5/2}$, implying that Mo was in the form of Mo^{4+} oxidation state [48]. Similarly, there could be fitted into two peaks at 163.3 and 162.2 eV for S 2p spectra, as revealed in Fig. 3e, which were separately belonging to S $2p_{1/2}$ and S $2p_{2/3}$, suggesting that S was in the form of S^{2-} [44]. The results of

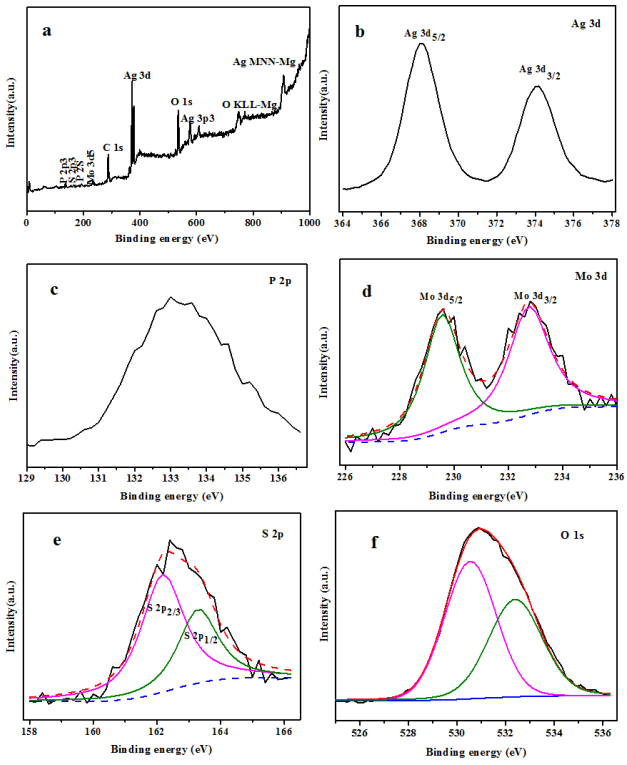

Fig. 3 XPS spectra of Ag_3PO_4/MoS_2 nanocomposite photocatalyst (a) survey spectrum, (b) Ag 3d, (c) P 2p, (d) Mo 3d, (e) S 2p and (d) O 1s.

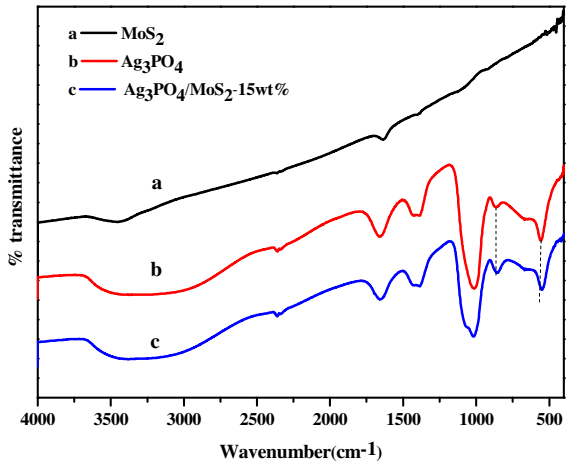

Fig. 4 FT-IR spectra of (a) pure MoS_2, (b) pure Ag_3PO_4 and (c) Ag_3PO_4/MoS_2 composite.

XPS spectra of Mo 3d and S 2p indicated the existence of MoS_2 in the composites. Regarding the O 1s spectra displayed in Fig. 3f, the binding energy of *ca.* 530.5 eV was ascribed to the O^{2-} anion in the Ag_3PO_4, while the peak at *ca.* 532.4 eV probably corresponded to the hydroxyl group [49]. Above discussion demonstrated the surface character of the composite catalyst, which was coincident well with the XRD and TEM results.

3.1.4 Fourier Transform Infrared Spectroscopy (FT-IR)

A comparison of Ag_3PO_4/MoS_2 composite to pure Ag_3PO_4 and MoS_2 in functional groups of chemical structure was monitored by FT-IR spectroscopy, as displayed in Fig. 4. For pure MoS_2 (Fig. 4a), the characteristic peak at 470 cm^{-1} was ascribed to the stretching vibrational mode of Mo-S in MoS_2, while the other two peaks at ca. 3446 and 1632 cm^{-1} were respectively corresponding to the stretching vibrations of -OH and H_2O molecules adsorbed on the surface of photocatalysts and bending vibration of -OH [50]. For pure Ag_3PO_4 (Fig. 4b), two peaks at *ca.* 3445 and 1652 cm^{-1} were related to the -OH stretching and bending vibration of adsorbed H_2O molecules. The peak at *ca.* 560 cm^{-1} was ascribed to the O=P-O bending vibration, while the peaks at *ca.* 850 and 1015 cm^{-1} were respectively assigned to the symmetric and asymmetric stretching vibrations of P-O-P rings [51]. All above characteristic bands were from PO_4^{3-} functional groups. In the case of Ag_3PO_4/MoS_2 composite with 15wt% of MoS_2 (Fig. 4c), the typical bands for Ag_3PO_4 still remained and no absorption bands characteristic of MoS_2 were observed, which may be resulting from the relatively small amounts and weak intensities. Interestingly, the characteristic peak of Ag_3PO_4/MoS_2 composite at *ca.* 560 cm^{-1} was shifted slightly compared with that of pure Ag_3PO_4, which indicated the interaction between Ag_3PO_4 nanoparticles and MoS_2 nanosheets. The interaction between Ag_3PO_4 and MoS_2 may benefit the photogenerated electron transfer and then improved the photocatalytic activity of composites.

3.1.5 BET Analysis

Photocatalytic oxidation is an interfacial reaction, so a larger specific surface area, which is useful for adsorption of organic compounds and providing more active sites for the photocatalytic process, usually contributed to the enhancement of photocatalytic activity. The adsorption of organic compounds on the surface of photocatalyst is the initial step in the decomposition

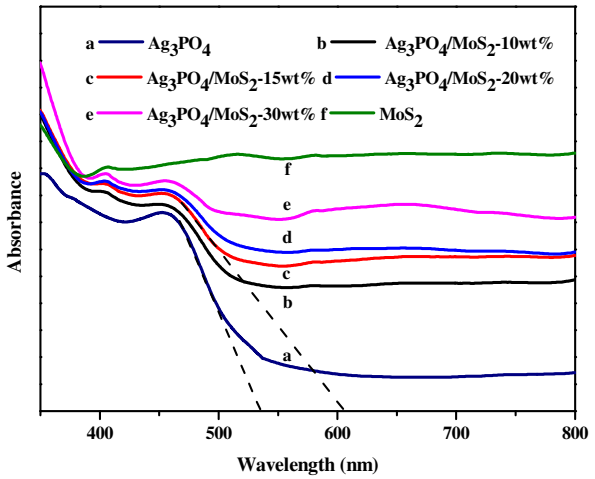

Fig. 5 UV-vis DRS of pure Ag_3PO_4, MoS_2 and Ag_3PO_4/MoS_2 composites with different content of MoS_2.

of organic compounds [33]. Table S1† showed the specific surface areas of the as-prepared samples investigated by nitrogen adsorption-desorption analysis. It could be clearly observed that the specific surface area of MoS_2 was much higher than that of pure Ag_3PO_4. Meanwhile, with the increasing content of MoS_2, the specific surface area of Ag_3PO_4/MoS_2 increased gradually, which was induced by the addition of 3D MoS_2 nanoarchitectures and the relatively better dispersion of Ag_3PO_4 nanoparticles. The high surface area was one of the factors that influenced the photocatalytic performance of hybrid composites under visible light irradiation.

3.1.6 Optical absorption properties

The optical absorption property is a key factor to select photocatalysts, hence UV-vis diffuse reflectance spectra is employed to determine the optical properties of the as-prepared samples. Fig. 5 demonstrated the DRS of Ag_3PO_4, MoS_2 and Ag_3PO_4/MoS_2 composites. The pure Ag_3PO_4 showed a sharp fundamental absorption edge at about 535 nm, in accordance with that reported by Yi et al [24]. Obviously, with the increasing content of MoS_2, the hierarchical Ag_3PO_4/MoS_2 composites showed enhanced absorption intensity in the visible light region, and it was consistent with that the color of the samples changed from yellow to gray when more black MoS_2 was introduced into the system. Compared with Ag_3PO_4, the reflectance of the composites showed a red shift, which was possibly due to the addition of the MoS_2 and the coupling together of the two materials, which was in keeping with the results of FT-IR. The red-shift meant a lower band gap, which was likely to facilitate electronic transitions [39]. Therefore, the light harvesting efficiency of the Ag_3PO_4/MoS_2 samples was higher than that of pure Ag_3PO_4 in the visible light region, and then produced more photogenerated electron-hole pairs to participate in the photodegradation process, which would be favorable for the photocatalytic activity.

3.2 Photocatalytic performance

On the basis of the above results, the photocatalytic activity of the as-synthesized samples is evaluated via the photodegradation of RhB under visible light irradiation, as shown in Fig. 6a. A blank test confirmed that the self-photolysis of RhB was negligible, and no significant degradation of RhB was observed with pristine MoS_2 catalyst under irradiation. These observations proved that RhB was decomposed by nanocomposite photocatalysts. By comparison with pure Ag_3PO_4, all Ag_3PO_4/MoS_2 composites with different content of MoS_2 showed appreciably much higher photocatalytic efficiency for photodegradation of RhB. Notably, the MoS_2 content had a crucial influence on the photocatalytic activity of the hierarchical Ag_3PO_4/MoS_2 composites, and the photocatalytic efficiency of the composites increased remarkably with increasing MoS_2 content, among which the Ag_3PO_4/MoS_2-15wt% composite exhibited the optimal photocatalytic activity, approximately 100% of the RhB was eliminated from the solution in 30 min, while pure Ag_3PO_4 only degraded about 55% of the RhB. Besides, the Ag_3PO_4/MoS_2-15wt% composite show better photocatalytic activity than the corresponding mechanical mixture one, and this suggested that there should exist interaction between Ag_3PO_4 and MoS_2. However, further increasing the amount of MoS_2 when the MoS_2 content was 15 wt%, it would lead to the decrease of photocatalytic activity. This may be because excess MoS_2 would hinder the light from contacting the Ag_3PO_4 nanoparticles and perhaps cover partial reactive sites of Ag_3PO_4 nanoparticles [52]. Due to the demands of both charge separation and light harvesting, the photocatalytic activity of Ag_3PO_4/MoS_2 first increased and then decreased with increasing MoS_2 ratio, and similar results were reported in the literature [53]. These results revealed that the synergistic effect between MoS_2 and Ag_3PO_4 played an important role in raising the photocatalytic properties under visible light irradiation.

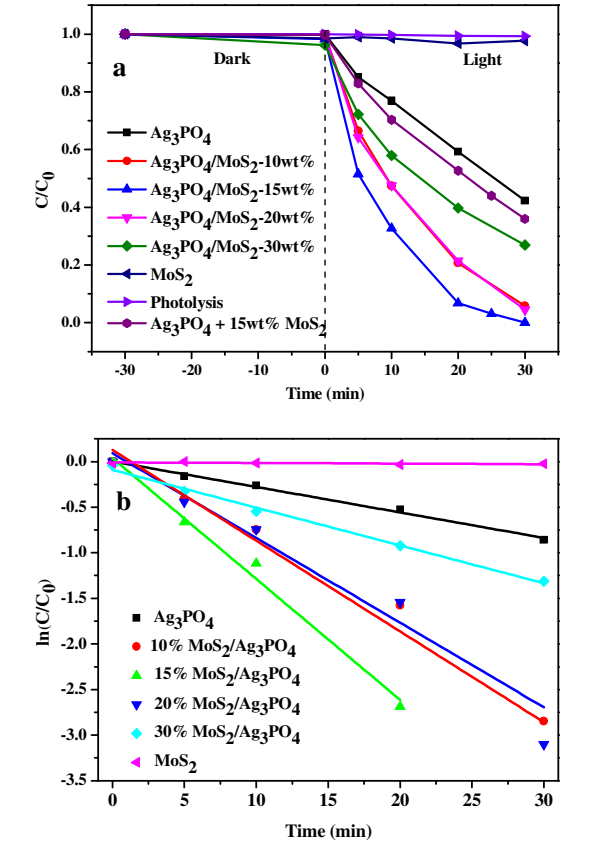

Fig. 6 (a) Photocatalytic efficiency of pristine Ag_3PO_4, MoS_2 and Ag_3PO_4/MoS_2 composites for RhB solution, (b) Kinetics of RhB degradation over the as-synthesized photocatalysts.

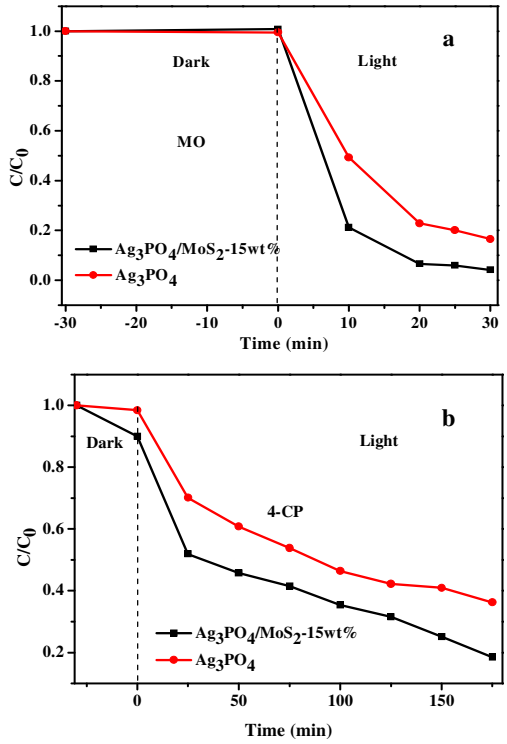

Fig. 7 Photodegradation efficiency of MO (a) and 4-CP (b) over Ag_3PO_4 and Ag_3PO_4/MoS_2-15wt% composite.

Moreover, the photodegradation of RhB was found to follow pseudo-first-order kinetics model lnC/C_0=-kt, where C is the concentration of reactant, t is the reaction time, and k is the rate constant. The linear relationship was shown in Fig. 6b, and the related information was summarized in Table S2†. It could be clearly seen that the rate constant of Ag_3PO_4/MoS_2-15wt% was larger than those of pure Ag_3PO_4 and other Ag_3PO_4/MoS_2 samples, which suggested the presence of a synergistic effect between the two components. Among which, the apparent rate constant of Ag_3PO_4/MoS_2-15wt% (0.133 min^{-1}) was the highest, and it was almost 4.8 times higher than that of pure Ag_3PO_4 (0.028 min^{-1}).

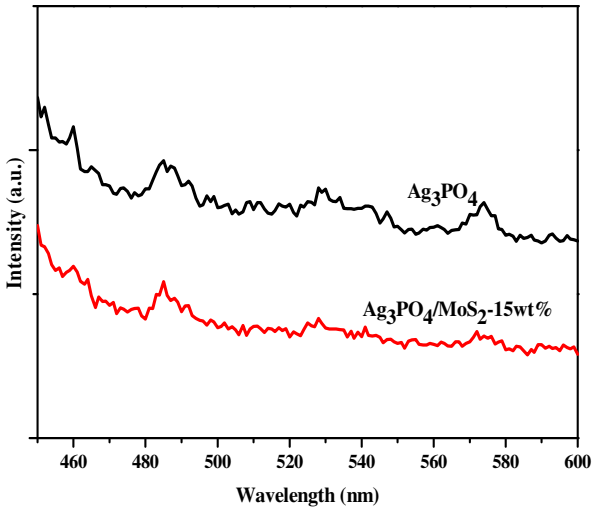

Fig. 8 Photoluminescence emission spectra of pure Ag_3PO_4 and Ag_3PO_4/MoS_2 composite.

In order to test the extensive adaptability, the photodegradation of methyl orange (MO, anionic dye) and colorless p-chlorophenol (4-CP, nonionic dye) was investigated by the Ag_3PO_4/MoS_2-15wt% composite photocatalyst under visible light irradiation. Fig. 7 exhibited the comparison results between Ag_3PO_4 and Ag_3PO_4/MoS_2-15wt% composite for decomposition of MO and 4-CP. The Ag_3PO_4/MoS_2-15wt% composite showed better photocatalytic activity than pure Ag_3PO_4, and it could completely degrade the MO solution within 30 min. Even 75% of the 4-CP solution, which was hard to be decomposed, could be degraded in 175 min. According to the photodegradation efficiency of the composites toward above three kinds of organic compounds, it could be concluded that the hierarchical Ag_3PO_4/MoS_2 composites show a relatively wide range of applications in the photodegradation field using solar energy.

3.3 Photoluminescence (PL)

A PL spectrum could be used for the material to show the dynamics of separation and recombination of photogenerated electron-hole pairs, because the recombination of excited electrons and holes gives rise to the PL emission signal [54]. Fig. 8 presented the PL spectra of pure Ag_3PO_4 and Ag_3PO_4/MoS_2-15wt% composite at room temperature, which was obtained at an excitation wavelength of 360 nm. For pure Ag_3PO_4, there were two distinct emission peaks at *ca.* 485 and 574 nm, which was pertinent with the recombination of the photo-generated holes with electrons around the surface oxygen vacancy [55]. It was found that the PL emission spectra of Ag_3PO_4/MoS_2 photocatalyst show the main peaks at similar positions but with different intensities, and it was lower than that of pure Ag_3PO_4, which implied that the recombination of photo-induced electrons and holes was effectively prevented in the hierarchical Ag_3PO_4/MoS_2 composite after the introduction of MoS_2 due to their matching band potentials. The analogous phenomenon had also been observed in other similar systems [56]. Therefore, it was not surprising that the photodegradation efficiency of RhB dyes over the heterojunction composites was much better. This result means that the hybrid composites with matched energy band positions could be promising photocatalysts for environmental applications.

3.4 Reusability

Apart from the photocatalytic performance, it is rather crucial to evaluate the stability of the composite photocatalysts from the view of practical application. As described in Fig. 9a, the recycle experiments were carried out to compare the reuse of Ag_3PO_4 particles and Ag_3PO_4/MoS_2 nanocomposites under visible light irradiation. It was well known that pure Ag_3PO_4 would photochemically decomposed if no sacrificial reagent was involved in the process, and the photodegradation for RhB of pure Ag_3PO_4 greatly decreased after 3 times cycling runs, of which the removal efficiency for RhB decreased by 36%. More importantly, the Ag_3PO_4/MoS_2 composites were detected to be more stable than pure Ag_3PO_4 in the photodegradation process, and the photocatalytic activity of Ag_3PO_4/MoS_2 composites was retained at over about 85% of its original activity after 3 successive recycling runs, which was still much higher than that of Ag_3PO_4. This result was in good agreement with the outcome of PL spectra. The slight drop of photo-activity may be mainly ascribed to two factors, inevitably reduction of partial Ag^+ to Ag^0 species and a carbon deposit formed on the surface of catalysts during the

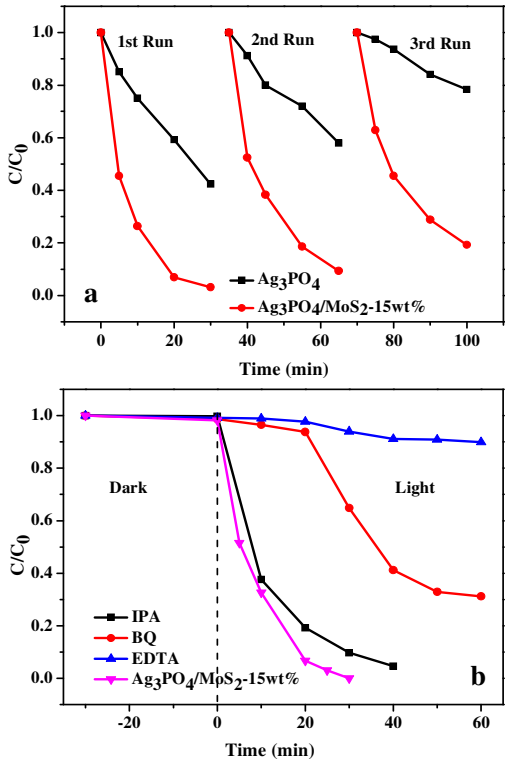

Fig. 9 (a) Cyclic performance of catalysts Ag_3PO_4/MoS_2 and Ag_3PO_4 for the photodegradation of RhB under visible light irradiation. (b) Effects of various scavengers on the visible light photocatalytic activity of Ag_3PO_4/MoS_2 -15wt% composite.

decomposition process [47], as observed in Fig. S3. When Ag_3PO_4 nanoparticals were deposited on the surface of MoS_2 nanoflakes, some of the electrons formed on the CB of Ag_3PO_4 could be captured by MoS_2 because of the conductivity of MoS_2 and the conjugation effect between photogenerated electrons and unsaturated sulfur atoms of the margin of MoS_2 [57], and then the photocorrosion of the Ag_3PO_4 would be suppressed to some extent. These factors all contributed to the improvement of the stability of Ag_3PO_4. Furthermore, the presence of MoS_2 would lead to more superoxide radical to get involved in the photo-oxidation process as MoS_2 was a sort of good O_2-activation cocatalyst [1].

3.4 Detection of reactive oxidative species

To further research the photocatalytic pathway of the degradation process, the trapping experiments of the composites were conducted to determine the main reactive species. In this study, isopropanol (IPA), ethylenediaminetetraacetic acid (EDTA) and benzoquinone (BQ) were served as hydroxyl radical (•OH) scavenger, hole (h^+) scavenger and superoxide radical ($•O_2^-$) scavenger, respectively [58]. As indicated in Fig. 9b, the degradation efficiency of RhB was slightly decreased upon addition of IPA, and nearly the same as that initial activity in the absence of scavengers. On the contrary, when EDTA or BQ were added, the photodegradation rate for RhB was seriously inhibited, suggesting that •OH were not the main active species of the hierarchical Ag_3PO_4/MoS_2 composites, but the $•O_2^-$ and h^+ were playing an important role in the decomposition of RhB under visible light irradiation.

3.5 Proposed mechanism

Due to the more negative potential of $O_2/•O_2^-$ [29], it's hard for the photogenerated electrons, in the CB of Ag_3PO_4, to reduce O_2 to super-oxygen anion. Based on the above experimental facts and analysis, a possible *Z*-scheme photocatalytic mechanism of the hierarchical Ag_3PO_4/MoS_2 composites with enhanced stability and photodegradation efficiency for RhB stemming from the synergistic effects between Ag_3PO_4 and MoS_2 was proposed and depicted in Fig. 10. Under visible light irradiation, both Ag_3PO_4 and MoS_2 could be excited to produce electrons and holes simultaneously due to their narrow band gap. The photoinduced charge carriers of Ag_3PO_4 were likely to recombine quickly without addition of MoS_2, causing the relatively low photocatalytic activity. According to the previous reports, the conduction band (CB) position and valance band (VB) position of MoS_2 are all higher than that of Ag_3PO_4, hence MoS_2 and Ag_3PO_4 have suitable band structure to form a heterojunction. After introducing 3D MoS_2 nanostructures, the electrons in the CB of Ag_3PO_4 go to the VB of MoS_2 and combine with holes there. The electrons in the CB of MoS_2 could be trapped by surface adsorbed oxygen of the hierarchical composite to yield $•O_2^-$ radicals, and then react with organic compounds. While the holes in the VB of Ag_3PO_4 could directly oxidize the organic compounds into CO_2, H_2O and other intermediates. Moreover, the MoS_2 could serve as electron capturer owing to its conductivity, which was also responsible for the improvement of photoactivity and stability. The following equations depicted the feasible prime reaction steps involved in the process of photodegradation for RhB.

$$Ag_3PO_4/MoS_2 + h\nu \text{ (visible light)} \rightarrow Ag_3PO_4/MoS_2\ (h^+ + e^-) \quad (1)$$

$$Ag_3PO_4\ (e^-) + MoS_2\ (h^+) \rightarrow Ag_3PO_4 + MoS_2 \quad (2)$$

$$MoS_2 + Ag_3PO_4\ (e^-) \rightarrow MoS_2\ (e^-) + Ag_3PO_4 \quad (3)$$

$$O_2 + MoS_2\ (e^-) \rightarrow •O_2^- + MoS_2 \quad (4)$$

$$RhB + •O_2^- \rightarrow\rightarrow CO_2 + H_2O + \text{other products} \quad (5)$$

$$RhB + Ag_3PO_4\ (h^+) \rightarrow\rightarrow CO_2 + H_2O + \text{other products} \quad (6)$$

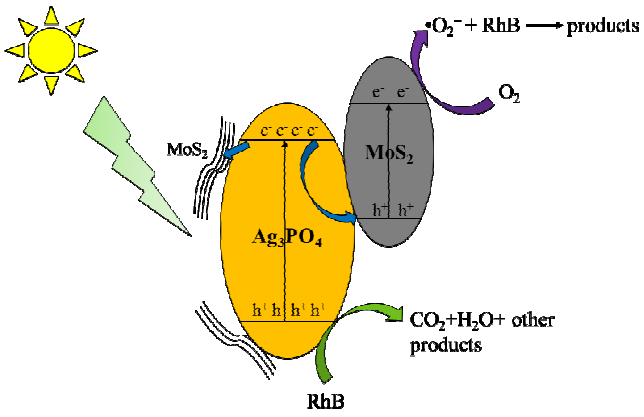

Fig. 10 Schematic diagram of possible photo-induced electron-hole pairs separation process and the feasible photodegradation mechanism of RhB over hierarchical Ag_3PO_4/MoS_2 nanocomposite.

4. Conclusion

In summary, a series of hierarchical Ag_3PO_4/MoS_2 composites with varied content of 3D flower-like spherical MoS_2 were successfully prepared. The hierarchical Ag_3PO_4/MoS_2 composites showed an enhanced photocatalytic performance than pure Ag_3PO_4. Among which, the heterojunction composite consisting of 15 wt% MoS_2 exhibited an excellent photocatalytic degradation for RhB, dramatically higher than other composites, and it also displayed better photoactivity toward degradation of MO and 4-CP. Furthermore, the Ag_3PO_4/MoS_2 composite revealed better stability than pure Ag_3PO_4 due to the function of MoS_2 as electron collectors. Radical trapping experiments indicated that the photodegradation of RhB over the as-synthesized composite was mainly via holes and superoxide radicals. This study demonstrates that layered MoS_2 could be used in designing novel and highly efficient visible-light-driven seminconductor photocatalysts for environmental remediation.

Acknowledgements

We would like to thank financial support by the Major State Basic Resource Development Program (Grant No. 2012CB224804), NSFC (Project 21373054, 21173052), the Natural Science Foundation of Shanghai Science and Technology Committee (08DZ2270500). The authors also thank the reviewer's valuable suggestion for the proposed Z-scheme mechanism in this work.

Notes and references

[a]*Department of Chemistry and Shanghai Key Laboratory of Molecular Catalysis and Innovative Materials, Fudan University, Shanghai 200433,P. R. China. Fax: (+86-21) 55665572; Tel: (+86-21) 55664678; E-mail: wldai@fudan.edu.cn*

†Electronic Supplementary Information (ESI) available: [details of any supplementary information available should be included here]. See DOI: 10.1039/x0xx00000x

1 Q. J. Xiang, J. G. Yu and M. Jaroniec, *Chem. Soc. Rev.*, 2012, **41**, 782-796.
2 A. Kudo and Y. Miseki, *Chem. Soc. Rev.*, 2009, **38**, 253-278.
3 J. Schneider, M. Matsuoka, M. Takeuchi, J. L. Zhang, Y. Horiuchi, M. Anpo and D. W. Bahnemann, *Chem. Rev.*, 2014, **114**, 9919-9986.
4 X. B. Chen and C. Burda, *J. Am. Chem. Soc.*, 2008, **130**, 5018-5019.
5 X. B. Chen, S. H. Shen, L. J. Guo and S. S. Mao, *Chem. Rev.*, 2010, **110**, 6503-6570.
6 G. Liu, Y. N. Zhao, C. H. Sun, F. Li, G. Q. Lu and H. M. Cheng, *Angew. Chem. Int. Ed.*, 2008, **47**, 4516-4520.
7 Z. F. Bian, T. Tachikawa, P. Zhang, M. Fujitsuka and T. Majima, *J. Am. Chem. Soc.*, 2014, **136**, 458–465.
8 Q. Li, B. D. Guo, J. G. Yu, J. R. Ran, B. H. Zhang, H. J. Yan and J. R. Gong, *J. Am. Chem. Soc.*, 2011, **133**, 10878-10884.
9 D. Chen and J. H. Ye, Adv. Funct. Mater., 2008, **18**, 1922-1928.
10 J. Yang, X. H. Wang, X. L. Zhao, J. Dai and S. R. Mo, *J. Phys. Chem. C*, 2015, **119**, 3068-3078.
11 J. L. Long, S. C. Wang, H. J. Chang, B. Z. Zhao, B. T. Liu, Y. G. Zhou, W. Wei, X. X. Wang, L. Huang and W. Huang, *Small*, 2014, **10**, 2791-2795.
12 L. Z. Zhang, D. W. Jing, L. J. Guo and X. D. Yao, *ACS Sustainable Chem. Eng.*, 2014, **2**, 1446-1452.
13 R. G. Li, H. X. Han, F. X. Zhang, D. Wang and C. Li, *Energy Environ. Sci.*, 2014, **7**, 1369-1376.
14 H. F. Cheng, B. B. Huang and Y. Dai, *Nanoscale*, 2014, **6**, 2009-2026.
15 J. Hu, S. X. Weng, Z. Y. Zheng, Z. X. Pei, M. L. Huang and P. Liu, *J. Hazard. Mater.*, 2014, **264**, 293-302.
16 Z. W. Zhao, Y. J. Sun and F. Dong, *Nanoscale*, 2015, **7**, 15-37.
17 D. L. Jiang, L. L. Chen, J. J. Zhu, M. Chen, W. D. Shi and J. M. Xie, *Dalton Trans.*, 2013, **42**, 15726-15734.
18 F. F. Shi, L. L. Chen, C. S. Xing, D. L. Jiang, D. Li and M. Chen, *RSC Adv.*, 2014, **4**, 62223-62229.
19 H. T. Ren, S. Y. Jia, Y. Wu, S. H. Wu, T. H. Zhang and X. Han, *Ind. Eng. Chem. Res.*, 2014, **53**, 17645-17653.
20 D. L. Jiang, L. L. Chen, J. M. Xie and M. Chen, *Dalton Trans.*, 2014, **43**, 4878-4885.
21 Y. F. Li, L. Fang, R. X. Jin, Y. Yang, X. Fang, Y. Xing and S. Y. Song, *Nanoscale*, 2015, **7**, 758-764.
22 H. G. Yu, L. L. Xu, P. Wang, X. F. Wang and J. G. Yu, *Appl. Catal. B: Environ.*, 2014, **144**, 75-82.
23 D. Reddy, S. Lee, J. Choi, S. Park, R. Ma, H. Yang and T. K. Kim, *Appl. Sur. Sci.*, 2015, **341**, 175-184.
24 Z. G. Yi, J. H. Ye, N. Kikugawa, T. Kako, S. X. Ouyang, H. Stuartwilliams, H. Yang, J. Y. Cao, W. J. Luo, Z. S. Li, Y. Liu and R. L. Withers, *Nat. Mater.*, 2010, **9**, 559-564.
25 H. Wang, Y. S. Bai, J. T. Yang, X. F. Lang, J. H. Li and L. Guo, *Chem. Eur. J.*, 2012, **18**, 5524-5529.
26 B. J. Zheng, X. Wang, C. Liu, K. Tan, Z. X. Xie and L. S. Zheng, *J. Mater. Chem. A*, 2013, **1**, 12635-12640.
27 C. Dinh, T. Nguyen, F. Kleitz and T. Do, *Chem. Commun.*, 2011, **47**, 7797-7799.
28 X. F. Yang, H. Y. Cui, Y. Li, J. L. Qin, R. X. Zhang and H. Tang, *ACS Catal.*, 2013, **3**, 363-369.
29 Y. S. Xu and W. D. Zhang, *Dalton Trans.*, 2013, **42**, 1094-1101.
30 J. Q. Zhang, K. Yu, Y. F. Yu, L. L. Lou, Z. Q. Yang, J. W. Yang and S. X. Liu, *J. Mol. Catal. A: Chem.*, 2014, **391**, 12-18.
31 H. Xu, C. Wang, Y. H. Song, J. X. Zhu, Y. G. Xu, J. Yan, Y. X. Song and H. M. Li, *Chem. Eng. J.*, 2014, **241**, 35-42.
32 W. S. Wang, H. Du, R. X. Wang, T. Wen and A. W. Xu, *Nanoscale*, 2013, **5**, 3315-3321.
33 S. Kumar, T. Surendar, A. Baruahb and V. Shanker, *J. Mater. Chem. A*, 2013, **1**, 5333-5340.
34 D. L. Jiang, J. J. Zhu, M. Chen and J. M. Xie, *J. Colloid Interface Sci.*, 2014, **417**, 115-120.
35 M. Chhowalla, H. S. Shin, G. Eda, L. J. Li, K. P. Loh and H. Zhang, *Nat. Chem.*, 2013, **5**, 263-275.
36 T. F. Jaramillo, K. P. Jorgensen, I. Bonde, J. H. Nielsen, S. Horch and I. Chorkendorff, *Science*, 2007, **317**, 100-102.
37 Y. Liu, Y. X. Yu and W. D. Zhang, *J. Phys. Chem. C*, 2013, **117**, 12949-12957.
38 M. Shen, Z. P. Yan, L. Yang, P. W. Du, J. Y. Zhang and B. Xiang, *Chem. Commun.*, 2014, **50**, 15447-15449.
39 J. Di, J. X. Xia, Y. P. Ge, L. Xu, H. Xu, J. Chen, M. Q. He and H. M. Li, *Dalton Trans.*, 2014, **43**, 15429-15438.
40 J. Z. Li, K. Yu, Y. H. Tan, H. Fu, Q. F. Zhang, W. T. Cong, C. Q. Song, H. H. Yin and Z. Q. Zhu, *Dalton Trans.*, 2014, **3**, 13136-13144.
41 Y. J. Chen, G. H. Tian, Y. H. Shi, Y. T. Xiao and H. G. Fu, *Appl. Catal. B: Environ.*, 2015, **164**, 40-47.
42 H. Katsumata, T. Sakai, T. Suzuki and S. Kaneco, *Ind. Eng. Chem. Res.*, 2014, **53**, 8018-8025.
43 R. H. Wei, H. B. Yang, K. Du, W. Y. Fu, Y. M. Tian, Q. J. Yu, S. K. Liu, M. H. Li and G. T. Zou, *Mater. Chem. Phys.*, 2008, **108**, 188-191.
44 J. H. Liu, L. Zhang, N. X. Li, Q. W. Tian, J. C. Zhou and Y. M. Sun, *J. Mater. Chem. A*, 2015, **3**, 706-712.
45 M. Y. Zhang, L. Li and X. T. Zhang, *RSC Adv.*, 2015, **5**, 29693-29697.
46 Y. H. Song, Y. C. Lei, H. Xu, C. Wang, J. Yan, H. Z. Zhao, Y. G. Xu, J. X. Xia, S. Yin and H. M. Li, *Dalton Trans.*, 2015, **44**, 3057-3066.
47 Y. Y. Chai, L. Wang, J. Ren and W. L. Dai, *Appl. Sur. Sci.*, 2015, **324**, 212-220.

48 R. Y. Zheng, L. Lin, J. L. Xie, Y. X. Zhu and Y. C. Xie, *J. Phys. Chem. C*, 2008, **112**, 15502-15509.
49 D. J. Wang, Z. H. Li, L. W. Shang, J. W. Liu and J. Shen, *Thin Solid Films*, 2014, **551**, 8-12.
50 D. Q. Gao, M. S. Si, J. Y. Li, J. Zhang, Z. P. Zhang, Z. L. Yang and D. S. Xue, *Nanoscale Res. Lett.*, 2013, **129**, 1-8.
51 B. Chai, J. Li and Q. Xu, *Ind. Eng. Chem. Res.*, 2014, **53**, 8744-8752.
52 Q. J. Xiang, J. G. Yu and M. Jaroniec, *J. Am. Chem. Soc.*, 2012, **134**, 6575-6578.
53 J. Fu, Y. L. Tian, B. B. Chang, F. N. Xi and X. P. Dong, *J. Mater. Chem.*, 2012, **22**, 21159-21166.
54 J. Tian, Y. H. Sang, Z. H. Zhao, W. J. Zhou, D. Z. Wang, X. L. Kang, H. Liu, J. Y. Wang, S. W. Chen, H. Q. Cai and H. Huang, *Small*, 2013, **9**, 3864-3872.
55 Q. H. Liang, Y. Shi, W. J. Ma, Z. Li and X. M. Yang, *Phys. Chem. Chem. Phys.*, 2012, **14**, 15657-15665.
56 Y. D. Hou, A. B. Laursen, J. S. Zhang, G. G. Zhang, Y. S. Zhu, X. C. Wang, S. Dahl an I. Chorkendorff, *Angew. Chem., Int. Ed.*, 2013, **52**, 3621-3625.
57 K. Chang, Z. W. Mei, T. Wang, Q. Kang, S. X. Ouyang and J. H. Ye, *ACS Nano*, 2014, **8**, 7078-7087.
58 W. L. Shi, F. Guo, J. B. Chen, G. B. Che and X. Lin, *J. Alloys Compd.*, 2014, **612**, 143-148.

Graphical Abstract